



Article

Significance of Free Convection Flow over an Oscillating Inclined Plate Induced by Nanofluid with Porous Medium: The Case of the Prabhakar Fractional Approach

Ali Raza ^{1,2}, Umair Khan ^{3,4} , Sayed M. Eldin ⁵ , Abeer M. Alotaibi ⁶, Samia Elattar ⁷ , Ballajja C. Prasannakumara ^{8,*} , Nevzat Akkurt ⁹ and Ahmed M. Abed ^{10,11}

¹ Department of Mathematics, University of Engineering and Technology, Lahore 54890, Pakistan

² Department of Mathematics, Minhaj University, Lahore 54770, Pakistan

³ Department of Mathematical Sciences, Faculty of Science and Technology, Universiti Kebangsaan Malaysia, UKM, Bangi 43600, Selangor, Malaysia

⁴ Department of Mathematics and Social Sciences, Sukkur IBA University, Sukkur 65200, Pakistan

⁵ Center of Research, Faculty of Engineering, Future University in Egypt, New Cairo 11835, Egypt

⁶ Department of Mathematics, Faculty of Science, University of Tabuk, P.O. Box 741, Tabuk 71491, Saudi Arabia

⁷ Department of Industrial & Systems Engineering, College of Engineering, Princess Nourah Bint Abdulrahman University, P.O. Box 84428, Riyadh 11671, Saudi Arabia

⁸ Department of Studies and Research in Mathematics, Davangere University, Davangere 577002, Karnataka, India

⁹ Department of Rare Earth Elements Application and Research Center, Munzur University, 62000 Tunceli, Turkey

¹⁰ Department of Industrial Engineering, College of Engineering, Prince Sattam Bin Abdulaziz University, Al-kharj 16273, Saudi Arabia

¹¹ Industrial Engineering Department, Faculty of Engineering, Zagazig University, Zagazig 44519, Egypt

* Correspondence: prasannakumarabc@davangereuniversity.ac.in



Citation: Raza, A.; Khan, U.; Eldin, S.M.; Alotaibi, A.M.; Elattar, S.; Prasannakumara, B.C.; Akkurt, N.; Abed, A.M. Significance of Free Convection Flow over an Oscillating Inclined Plate Induced by Nanofluid with Porous Medium: The Case of the Prabhakar Fractional Approach. *Micromachines* **2022**, *13*, 2019.

<https://doi.org/10.3390/mi13112019>

Academic Editors: Kwang-Yong Kim and Stéphane Colin

Received: 25 October 2022

Accepted: 17 November 2022

Published: 19 November 2022

Publisher's Note: MDPI stays neutral with regard to jurisdictional claims in published maps and institutional affiliations.



Copyright: © 2022 by the authors. Licensee MDPI, Basel, Switzerland. This article is an open access article distributed under the terms and conditions of the Creative Commons Attribution (CC BY) license (<https://creativecommons.org/licenses/by/4.0/>).

Abstract: Given the importance and use of electrically conducted nanofluids, this work aims to examine an engine-oil-based nanofluid including various nanoparticles. In the current study, a fractional model for inspecting the thermal aspect of a Brinkman-type nanofluid, composed of (molybdenum disulfide (MOS_2) and graphene oxide (GO) nanoparticles flows on an oscillating infinite inclined plate, which characterizes an asymmetrical fluid flow, heat, and mass transfer. Furthermore, the Newtonian heating effect, magnetic field, and slip boundary conditions were taken into account. The objectives for implementing the Prabhakar-like fractional model are justified because this fractional algorithm has contemporary definitions with no singularity restrictions. Furthermore, the guided fractional model was solved using the Laplace transform and several inverse methods. The obtained symmetrical solutions have been visually analyzed to investigate the physics of several relevant flow parameters on the governed equations. Some exceptional cases for the momentum field are compiled to see the physical analysis of the flowing fluid symmetry. The results show that the thermal enhancement can be progressively improved with the interaction of the molybdenum disulfide-engine oil-based nanofluid suspension, rather than with the graphene oxide mixed nanoparticle fluid. Furthermore, the temperature and momentum profiles enhance due to the factional parameters for molybdenum disulfide and the graphene oxide-engine oil-based nanofluid suspension. This study's graphical and numerical comparison with the existing literature has shown a very close resemblance with the present work, which provides confidence that the unavailable results are accurate. The results show that an increase improved the heat transmission in the solid nanoparticle volume fractions. In addition, the increment in the mass and heat transfer was analyzed in the numerical evaluation, while the shear stress was enhanced with the enhancement in the Prabhakar fractional parameter α .

Keywords: nanofluid; heat transfer; Brinkman-type fluid; Prabhakar fractional derivative; slip effects; Newtonian heating effect

1. Introduction

Due to the numerous uses for thermal energy across all industries, such as the biomedical and engineering fields, and the current exceptionally high demand for thermal energy, researchers have been motivated to accelerate the rate of thermal perturbation from the pending sources by the extraordinary vision of nano-science. Enhancement in heat effectiveness can have an advantage over solicitations incorporating the analysis of plasma, microelectronic equipment, such as nuclear reactors, space refrigeration, microchips in computers, power generation, and many more [1]. Non-Newtonian fluids possess broad applications in science and technology, such as in cosmetics, biochemical, and medical applications. Because of their extensive applications in different fields, investigators are constantly fascinated by these fluids [2,3]. Therefore, different models in the past for non-Newtonian fluids are studied. One of them is known as the Brinkman-type fluid, which Darcy introduced for those fluids that pass through small permeable surfaces [4]. More precisely, this fluid model is appropriate for the flow on a body with a negligible permeability. However, Darcy's law does not apply to the flow on a body or surfaces with a very high porosity. Using a fluid model across the porous surfaces was an idea put forth by Brinkman [5,6]. A viscous, incompressible fluid with a significant amount of porosity, is known as a Brinkman-type fluid. Minimal research in this regard, has been achieved, through the Brinkman-type fluid. In particular, convection flows with Brinkman-type fluid and heat and mass transmission are much less studied, while these investigations have abundant applications in many industries [7,8].

The sharp rise in energy claims worldwide has directed increased efforts to accomplish energy-effective arrangements. The use of innovative schemes to expand the thermal concert of heat exchangers is one of the furthestmost serious and modern subjects in the modern world. However, most of these approaches are accompanied by a rise in the pressure drop, called defect. Specifically, the enhancement procedure is hydraulic and thermally supportive [9]. Recently, nano-structure carbon mixtures, such as graphite, graphene, and some metals, such as molybdenum and magnesium, have been utilized to stock hydrogen gas. Nanofluids are simply latent heat-transmitting flowing liquids with enhanced thermophysical properties, and a heat transfer execution that may be used in various devices for more efficient operations. They are used to improve the thermal conductivity of base fluids, such as oil, ethylene glycol, water, propylene glycol, and so on, because they are poor heat-transmitting fluids. Temperature reduction, cancer treatment, and manufacturing use various biomedical and scientific engineering fields. Thermic conduction of a schematic heat-transporting fluid is enriched by the interruptions of significant molecules, which increases the heat transfer coefficient. Because solid metallic components have more thermic conduction than base fluids, suspended constituents are used to promote thermic conduction and heat transmission. The significant advantages of nanofluids are that they have a sufficient viscosity and are auxiliary stable with enhanced wetting, flowing, and diffusion characteristics along the solid surfaces, even for tiny immersion nanoparticles [10]. Srivastava et al. [11] investigated a biological population fractional model. The blended homotopy methods relating to the Sumudu transform are operated to find the solutions and show that the prey's population abruptly declines with time. Kumar et al. [12] derived a new numerical technique to obtain the numerical solution of fractional PDEs, including the Caputo–Fabrizio derivatives, compared their obtained numerical results with the analytical results, and determined that their anticipated numerical technique attains accurate results. Mahanthesh [13] numerically studied the nanofluid flow and heat transfer using the modified Buongiorno model. The author proved that the interruption of the nanoparticle's growth increases the thermal conduction and consequently expands the temperature. Rana et al. [14] investigated the flow of ethylene glycol-based titania nano liquid using the finite difference method, and noted that the accumulation of nanoparticles increases the temperature, and the velocity field is reduced. The finite difference scheme was used to examine the radiative flow of a polar nonliquid, along with a stretchable sheet in [15]. It was observed that the heat generation parameter has a decreasing impact on

the Nusselt number. The impact of the nanoparticle combination upon the 3D flow of the titanium nonliquid, because of an exponentially extended surface, was studied in [16], by the shooting method and showed that the impact of the magnetism is much more in the ordinary fluid than in the nanofluid. Abro et al. [17] studied the influences of the magnetized nanoparticles, analytically, on the natural convection flow of the nanofluid using the Laplace method. They proved that the improvement in volume fraction increases the thickness of the thermal boundary layer. For this article's sake, we incorporate new studies, based on the exact and numerical fractional approaches [18–25]. Shafee et al. [26] used computational methods to forecast the turbulent nanofluid (CuO/H₂O) flow and heat transfer, and showed that the inclusion of helical tabulator measurement enhances the core nanofluid movement. Farshad and Sheikholeslami [27] discussed the turbulent nanomaterial flow using the finite volume method and showed that by enhancing friction because of the increasing inlet velocity, the quantity of the Bejan number decreases. Hussanan et al. discussed and evaluated the MHD's inherently unstable flow of nanofluids passing through an accelerating upright plate, set in a porous medium [28]. Sheikholeslami et al. [29] investigated the effect of the persuaded magnetic flux on heat conduction using the KKL (Koo Kleinstreuer-Li) relationship on the nanofluid flow. Akyürek et al. [30] examined the experimentally turbulent forced convective thermal transmission, as well as the pressure drop properties of the nanofluids through a concentric tube. They proved that nanofluids with small particle concentrations did not demonstrate a significant impact on the pressure drop variation.

Fractional calculus is an appropriate tool to explain various anomalous dynamics and processes in complex media, in physics, rheology, and electrical engineering [31–36]. Fractional calculus techniques are also applied to evaluate the anomalous relaxation phenomena [37]. In current years, it has been determined that some fractional operators and non-singular kernels are anticipated. For instance, the Atangana–Baleanu derivative and the Mittag–Leffler kernel [38] have attracted a lot of attention. A fractional derivative with a Prabhakar-like kernel is recommended by Giusti and Colombaro [39], which is the most extensive form of the Atangana–Baleanu derivative. Mahanthesh et al. [40] studied an unsteady nonlinear Casson fluid and an oscillating plate, analytically, with the Laplace technique. They proved that the nonlinear convective flow has a substantial impact on heat, as well as mass transfer properties. Abro et al. [41] studied a fractional model of the unsteady natural convection radiating flow, along with the Fourier sine transform, and showed that enhancing the fractional parameter velocity has no symmetrical behavior. Saqib et al. [42] analyzed the Brinkman-type nanofluid with CNTs and ramped the temperature conditions. Khan et al. [43] discussed an advection–reaction diffusion fractional model numerically using the Laplace, forward Euler, and Lagrange interpolation methods. They delivered a base for their considered model's uniqueness, existence, and the HU-stability analysis. Abro et al. [44] investigated the thermal influences of the MHD micropolar fluid which was secreted by the Caputo–Fabrizio derivative. They found the exact solutions by applying the Fourier sine and the Laplace approach. They concluded that the velocity decreases while growing the magnetic parameters. Siddiqui et al. [45] studied the water-based ferrofluids, numerically, by employing a unique finite difference technique. They noted that the magnitude of the secondary vortices declines if the magnetic strength is boosted. Pandey et al. [46] discussed a space-time advection–reaction–diffusion fractional equation with the homotopy perturbation method. They presented that solute concentration when the considered system tended to move from the fractional-order to integer-order, in the existence of the sink and source terms. They claimed that their proposed method is more suitable for dealing with a fractional model, taking Mittag–Leffler's fractional derivative and estimating the motion of the diverse models ascending in various science and engineering disciplines. Ahokposi et al. [47] recently investigated the groundwater fractal flow with the fractional differentiation and the Mittag–Leffler rule. They employed three distinct numerical strategies: implicit, explicit, and the Crank–Nicholson approach. Khan et al. [48] focused on the flow of generalized Casson fluids with the fractional derivatives,

and discovered the closed-form solutions in the Wright function. Khan et al. [49] used the Caputo–Fabrizio derivatives in the heat transfer study of a Maxwell fluid in, another paper. This is an appealing research subject because of the major uses of nanofluids in cooling loads, solar thermal energy, electronic cooling, and solar energy engineering.

According to a review of the literature, as mentioned above, no studies have been carried out on the MHD Brinkman-type nanofluids (such as graphene oxide and molybdenum disulfide nanoparticles with a viscoelastic base fluid), using the Newtonian heating effect, slip boundary conditions, and our suggested setting, in combination with the Prabhakar time-fractional approach to obtain the better energy transfer phenomenon. To address this research gap, a Prabhakar time-fractional Brinkman-type fluid model for the flow of (MoS_2) and (GO) based nanoparticles under the influence of an externally inclined magnetic field, was investigated. According to the available literature, the integer order derivatives are local in nature, but the time-fractional derivatives are non-local and preserve the memory property. With such motivations, the current research attempts to offer Prabhakar with a fractional model for a nanofluid problem, involving multiple types of nanoparticles. A close thermal inspection of the modified nanofluid model is offered by applying molybdenum disulfide and graphene oxide nanoparticles with a viscoelastic base fluid. The comparative thermal data for these various nanoparticles is provided to further understand the energy thermal transfer mechanisms. The primary phrases and concepts of the Prabhakar fractional model are presented first, followed by the application of this novel technique in the simulated situation. In two respects, this study is innovative. It first demonstrates the application of the Prabhakar fractional model to various coupled differential systems. Second, this model confirms the thermal applications of different nanoparticles to improve the heating transportation. Furthermore, temperature, concentration, and velocity differences are depicted graphically to demonstrate the effect of the controlling factors.

2. Mathematical Formulation

Consider a free convection Brinkman-type nanofluid, mixed with (molybdenum disulfide, graphene oxide) nanoparticles and base engine oil fluid, moving over a poured infinite plate has been shown in Figure 1. The x -axis is drawn vertically up the plate, whereas the y -axis is orthogonal to it. The pressure gradient is supposed to be ignored in the presented model, and the moving fluid is electrically conducted. An angled magnetic field, sliding, and the Newtonian heating effects are also considered. Because the magnetic Reynolds number is assumed to be very small, the induced magnetic field is ignored, the base is assumed to be fluid, and the suspension nanoparticles are in the thermal equilibrium. At $t = 0$, both the plate and the combined fluid are at rest, with the ambient temperatures and concentrations T_∞ and C_∞ . Due to the increase in the temperature variation and the oscillations of the pored oscillating plate, the free convection develops after a brief interval of time $t > 0^+$, and the constant nanofluid begins to move on the inclined plate. The constant plate vibrates with the constant velocity $f(t)$, having some of its Laplace. We made the following assumptions.

- Except for the impact of the body action term, all fundamental fluid parameters are supposed to be fix.
- An applied magnetic field with a strength of B_0^2 is inclined with θ_1 as the inclination of the magnetic field.
- Because the fluid's conductivity is considered low, the magnetic Reynolds number is less than one, and the induced field is small, compared to the transverse magnetic field.
- It is also assumed that the temperature, concentration, and velocity depend on y and t .
- It is also assumed that there is still no applied voltage, since the electric field is nonexistent [50].
- Based on the above presumptions and Boussinesq's approximations [51], the governed equations can be stated as follows [42,50].

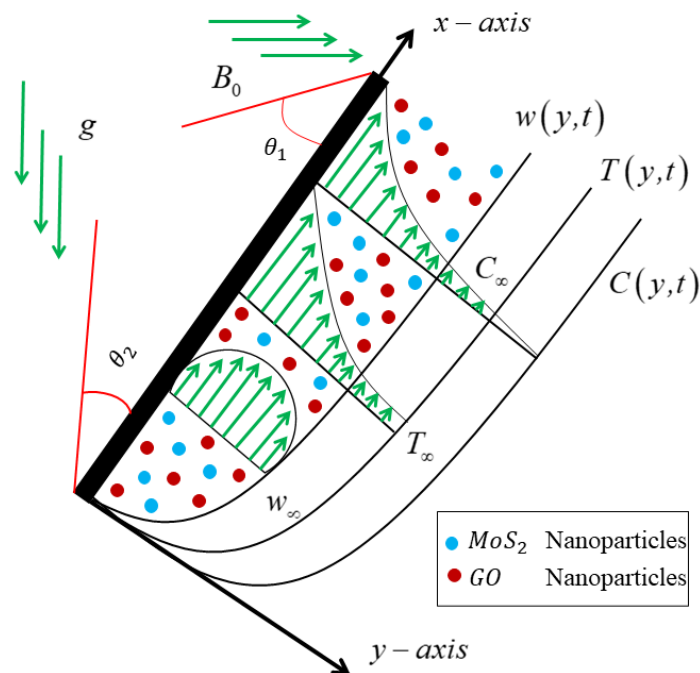


Figure 1. Physical model of the flow problem.

Momentum equation:

$$\begin{aligned} & \rho_{nf} \left(\frac{\partial w(y,t)}{\partial t} + \beta_1^* w(y,t) \right) \\ & = \mu_{nf} \frac{\partial^2 w(y,t)}{\partial y^2} - \sigma_{nf} B_0^2 \sin(\theta_1) w(y,t) - \frac{\mu_{nf}}{k} w(y,t) \\ & + g(\rho\beta_T)_{nf} \cos(\theta_2) (T(y,t) - T_\infty) \\ & + g(\rho\beta_c)_{nf} \cos(\theta_2) (C(y,t) - C_\infty) \end{aligned} \tag{1}$$

Thermal equation:

$$(\rho C_p)_{nf} \frac{\partial T(y,t)}{\partial t} = - \frac{\partial \delta(y,t)}{\partial y} \tag{2}$$

Fourier law of thermal flux:

$$\delta(y,t) = -k_{nf} \frac{\partial T(y,t)}{\partial y} \tag{3}$$

Diffusion balance equation:

$$\frac{\partial C(y,t)}{\partial t} = - \frac{\partial J(y,t)}{\partial y} \tag{4}$$

Fick's law:

$$J(y,t) = -D \frac{\partial C(y,t)}{\partial y} \tag{5}$$

Furthermore, the identical physical conditions are specified as [52,53]:

$$\begin{aligned} & w(y,0) = 0, \quad T(y,0) = T_\infty, \quad C(y,0) = C_\infty; \quad \forall y \geq 0 \\ & w(0,t) - h \frac{\partial w(y,t)}{\partial y} \Big|_{y=0} = U_o H(t) f(t), \quad \frac{\partial T(y,t)}{\partial y} \Big|_{y=0} = -\frac{b}{k} T(0,t) \quad C(0,t) = C_w; \quad t > 0 \\ & w(y,t) \rightarrow 0, \quad T(y,t) \rightarrow T_\infty, \quad C(y,t) \rightarrow C_\infty; \quad y \rightarrow \infty, \quad t > 0 \end{aligned}$$

where $w_{(y,0)}$ is the fluid velocity, ρ_{nf} symbolizes the effective density of the nanofluid, μ_{nf} is the effective dynamic viscosity of the nanofluid, B indicates the magnetic field, β_{Tnf} is the effective thermal volumetric coefficient, β_{Cnf} is the effective solutal volumetric coefficient, k_{nf} is the effective thermal conductivity, and D indicates the diffusion coefficient. The mathematical relations for $\rho_f, \mu_f, \sigma_f, k_f$ regular nanofluid parameters with different thermal characteristics are presented in Table 1.

Table 1. Model for the thermophysical properties of the nanofluid quantities [54].

Thermal Features	Nanofluid
Density	$\frac{\rho_{nf}}{\rho_f} = (1 - \varphi) + \varphi \frac{\rho_s}{\rho_f}$
Dynamic Viscosity	$\frac{\mu_{nf}}{\mu_f} = \frac{1}{(1-\varphi)^{2.5}}$
Thermal Expansion Coefficient	$\frac{(\rho\beta_T)_{nf}}{(\rho\beta_T)_f} = (1 - \varphi) + \varphi \frac{(\rho\beta_T)_s}{(\rho\beta_T)_f}$
Electrical Conductivity	$\frac{\sigma_{nf}}{\sigma_f} = \left(1 + \frac{3\left(\frac{\sigma_s}{\sigma_f} - 1\right)\varphi}{\left(\frac{\sigma_s}{\sigma_f} + 2\right) - \left(\frac{\sigma_s}{\sigma_f} - 1\right)\varphi} \right)$
Concentration Expansion Coefficient	$\frac{(\rho\beta_C)_{nf}}{(\rho\beta_C)_f} = (1 - \varphi) + \varphi \frac{(\rho\beta_C)_s}{(\rho\beta_C)_f}$
Thermal Conductivity	$\frac{k_{nf}}{k_f} = \left(\frac{k_s + (n-1)k_f - (n-1)(k_f - k_s)\varphi}{k_s + (n-1)k_f + (k_f - k_s)\varphi} \right)$
Heat Capacitance	$\frac{(\rho C_p)_{nf}}{(\rho C_p)_f} = (1 - \varphi) + \varphi \frac{(\rho C_p)_s}{(\rho C_p)_f}$

The subscripts nf, f, s in the above table denote nanofluid, base fluid, and solid, all regarded as separate nanoparticles. We implement the following non-dimensional quantities to non-dimensionalize the given unsteady problem:

$$w^* = \frac{w}{U_0}, \quad y^* = \frac{U_0 y}{\nu_f}, \quad t^* = \frac{t}{t_0}, \quad t_0 = \frac{\nu_f}{U_0^2}, \quad T^* = \frac{T_{(y,t)} - T_\infty}{T_w - T_\infty}, \quad q^* = \frac{q}{q_0},$$

$$J^* = \frac{J}{J_0}, \quad C^* = \frac{C_{(y,t)} - C_\infty}{C_w - C_\infty}, \quad h^* = \frac{U_0}{\nu_f} h, \quad \omega^* = \frac{\nu_f \omega}{U_0^2}$$

The non-dimensional restrictions indicated above, to reduce the number of variables in the controlled Equations (1)–(5) and ignoring the “*” notation, one obtains

$$\Lambda_0 \left(\frac{\partial w_{(y,t)}}{\partial t} + \beta_1 w_{(y,t)} \right) = \Lambda_1 \frac{\partial^2 w_{(y,t)}}{\partial y^2} - \Lambda_2 M \sin(\theta_1) w_{(y,t)} - \frac{\Lambda_1}{K} w_{(y,t)} + \Lambda_3 \cos(\theta_2) T_{(y,t)} + \Lambda_4 \cos(\theta_2) C_{(y,t)} \quad (6)$$

$$\Lambda_5 Pr \frac{\partial T_{(y,t)}}{\partial t} = \Lambda_6 \frac{\partial^2 T_{(y,t)}}{\partial y^2}, \quad (7)$$

$$Sc \frac{\partial C_{(y,t)}}{\partial t} = \frac{\partial^2 C_{(y,t)}}{\partial y^2}, \quad (8)$$

where the equivalent conditions are incorporated as

$$w_{(y,0)} = 0, \quad T_{(y,0)} = 0, \quad C_{(y,0)} = 0; \quad \forall y \geq 0 \quad (9)$$

$$w_{(0,t)} - h \frac{\partial w_{(y,t)}}{\partial y} \Big|_{y=0} = H(t) f(t), \quad \frac{\partial T_{(y,t)}}{\partial y} \Big|_{y=0} = -\left(1 + T_{(0,t)}\right) \quad C_{(0,t)} = 1; \quad t > 0 \quad (10)$$

$$w_{(y,t)} \rightarrow 0, \quad T_{(y,t)} \rightarrow 0, \quad C_{(y,t)} \rightarrow 0; \quad y \rightarrow \infty, \quad t > 0 \quad (11)$$

Equation (9) represents the constant fluid motion, thermal profile, and concentration field in the above-transformed conditions at $t = 0$, as supposed in the problem formulation

section. In Equation (10), the rate of the fluid flow with the constant fluid velocity $f(t)$ with slipping, the boundary effect is implemented. Furthermore, the thermal field rate with a constant concentration in the Newtonian heating effect is considered. Moreover, in the last boundary equation (11), the zero-fluid movement, temperature, and concentration at $y \rightarrow \infty$ are considered. Finally, the thermal features of the considered base fluid (engine oil) and the nanoparticles (molybdenum disulfide, graphene oxide) are examined in Table 2.

Table 2. Thermal properties of the base liquids and nanoparticles [55].

Material	Engine Oil	MoS ₂	GO
ρ (kg/m ³)	884	5060	1800
C_p (J/kg K)	1910	397.21	717
k (W/m K)	0.144	904.4	5000
β_T (K ⁻¹)	70×10^{-5}	2.8424×10^{-5}	0.284×10^{-5}
β_C (m ² h ⁻¹)	165.5×10^{-5}	2.05×10^{-5}	0.657×10^{-5}
σ (Ω m)	2.09×10^{-4}	2.09×10^{-4}	1×10^7
Pr	233	-	-

where:

$$Pr = \frac{\mu C_p}{\kappa_n}, \quad \beta_1 = \frac{v_f \beta_o^*}{U_o^2}, \quad Gr = \frac{g(v\beta_T)_f(T_w - T_\infty)}{U_o^3}, \quad M = \frac{\sigma_f v_f B_o^2}{\rho_f U_o^2}, \quad Sc = \frac{v_f}{D}, \quad K = \frac{kU_o}{v_f}$$

$$Gm = \frac{g(v\beta_C)_f(C_w - C_\infty)}{U_o^3}, \quad \Lambda_o = (1 - \varphi) + \varphi \frac{\rho_s}{\rho_f}, \quad \Lambda_1 = \frac{1}{(1 - \varphi)^{2.5}}, \quad \Lambda_2 = \frac{\sigma_{nf}}{\sigma_f}$$

$$\Lambda_3 = (1 - \varphi) + \varphi \frac{(\rho\beta_t)_s}{(\rho\beta_t)_f}, \quad \Lambda_4 = (1 - \varphi) + \varphi \frac{(\rho\beta_c)_s}{(\rho\beta_c)_f}, \quad \Lambda_5 = (1 - \varphi) + \varphi \frac{(\rho C_p)_s}{(\rho C_p)_f},$$

$$\Lambda_6 = \left(\frac{k_s + (n-1)k_f - (n-1)(k_f - k_s)\varphi}{k_s + (n-1)k_f + (k_f - k_s)\varphi} \right)$$

Signify the Prandtl number, Brinkman fluid parameter, heat Grashof number, mass Grashof number, inclined magnetic field, Schmidt number, dimensionless porosity parameter and $\Lambda_o, \Lambda_1, \Lambda_2, \Lambda_3, \Lambda_4, \Lambda_5, \Lambda_6$ are the constants raised during the mathematical calculations, respectively.

3. Prabhakar Fractional Derivative Scheme

A practical and contemporary mathematical fractional approach has been used in this work, from which the thermal memory effect may be examined. As a result, the Prabhakar fractional derivative is presented here, which is based chiefly on the modified Fourier’s and Fick’s laws of thermal conductivity [56]

$$\delta_{(y,t)} = -{}^C \mathcal{D}_{\alpha,\beta,\alpha}^\gamma \frac{\partial T_{(y,t)}}{\partial y} \tag{12}$$

$$J_{(y,t)} = -{}^C \mathcal{D}_{\alpha,\beta,\alpha}^\gamma \frac{\partial C_{(y,t)}}{\partial y} \tag{13}$$

where ${}^C \mathcal{D}_{\alpha,\beta,\alpha}^\gamma$ is the Prabhakar fractional derivative, which may be derived numerically [56,57]

$${}^C \mathcal{D}_{\alpha,\beta,\alpha}^\gamma h(t) = E_{\alpha,n,-\beta,\alpha}^{-\gamma} h^n(t) = \int_0^t (t - \tau)^{n-\beta-1} E_{\alpha,n-\beta}^{-\gamma} (\mathfrak{Q}(t - \tau)^\alpha) h^n(\tau) d\tau$$

where $h^{(n)}$ represents the n th derivative of $h(t) \in AC^n(0, b)$, $AC^n(0, b)$ and means a real-valued function that has continuous derivatives of the $(n - 1)$ order with interval $(0, b)$.

$$E_{\alpha, \beta, \vartheta}^{\gamma} h(t) = \int_0^t (t - \tau)^{\beta-1} E_{\alpha, \beta}^{-\gamma}(\vartheta(t - \tau)^{\alpha}) h(\tau) d\tau$$

is known as the Prabhakar integral with

$$E_{\alpha, \beta}^{\gamma}(z) = \sum_{m=0}^{\infty} \frac{\Gamma(\gamma + m) z^m}{m! \Gamma(\gamma) \Gamma(\alpha m + \beta)}, \quad \alpha, \beta, \gamma, z \in \mathbb{C}, \quad \text{Re}(\alpha) > 0$$

is three-dimensional, The MittagLeffler function, and $e_{\alpha, \beta}^{\gamma}(\alpha; t) = t^{\beta-1} E_{\alpha, \beta}^{\gamma}(\alpha t^{\alpha})$ is the Prabhakar kernel. The Prabhakar fractional derivative operator ${}^C \mathcal{D}_{\alpha, \beta, \vartheta}^{\gamma}$, the Laplace transform is given as

$$\mathcal{L} \left[{}^C \mathcal{D}_{\alpha, \beta, \vartheta}^{\gamma} h(t) \right] = \vartheta^{\beta-m} (1 - \vartheta \zeta^{-\alpha})^{\gamma} \mathcal{L} \{ h^m(t) \} \tag{14}$$

and by taking $\beta = \gamma = 0$ the classical Fourier law can also be obtained.

4. Solution of the Problem

4.1. Solution of the Temperature Profile

Because the criterion for is assumed to be $\beta \in [0, 1)$, use $m = 0$ in the preceding formula of Equation (14). Furthermore, for the temperature field solution, the Laplace transformation scheme on Equations (7) and (12) and its accompanying conditions are used

$$\Lambda_5 Pr s \bar{T}_{(y,s)} = -\Lambda_6 \frac{\partial \bar{\delta}_{(y,s)}}{\partial y} \tag{15}$$

$$\bar{\delta}_{(y,s)} = -s^{\beta} (1 - \alpha s^{-\alpha})^{\gamma} \frac{\partial \bar{T}_{(y,s)}}{\partial y} \tag{16}$$

$$\left. \frac{\partial \bar{T}_{(y,s)}}{\partial y} \right|_{y=0} = -\left(\frac{1}{s} + \bar{T}_{(0,s)} \right); \quad \bar{T}_{(y,s)} \rightarrow 0, \quad y \rightarrow \infty \tag{17}$$

By plugging Equation (16) into (15) and using the above-transformed conditions, the thermal profile may be solved as follows

$$\bar{T}_{(y,s)} = \frac{1}{\sqrt{\frac{\Lambda_5 Pr}{\Lambda_6} \frac{s^{1-\beta}}{(1-\alpha s^{-\alpha})^{\gamma}} - 1}} \frac{e^{-y \sqrt{\frac{\Lambda_5 Pr}{\Lambda_6} \frac{s^{1-\beta}}{(1-\alpha s^{-\alpha})^{\gamma}}}}}{s} \tag{18}$$

Tables 3 and 4 show that the Laplace inverse of the aforementioned thermal profile solution will be numerically investigated using the Stehfest and Tzou techniques.

4.2. Solution of the Concentration Profile

For the solution of the concentration of the boundary layers, using the LT on the non-dimensionalized and converted with the leading Equations (8) and (13), and using the result of Equation (11), the solution of $\bar{C}_{(y,s)}$ overcomes that.

$$Sc s \bar{C}_{(y,s)} = -\frac{\partial \bar{J}_{(y,s)}}{\partial y} \tag{19}$$

$$\bar{J}_{(y,s)} = -s^{\beta} (1 - \alpha s^{-\alpha})^{\gamma} \frac{\partial \bar{J}_{(y,s)}}{\partial y} \tag{20}$$

$$\bar{C}_{(0,s)} = \frac{1}{s}; \quad \bar{C}_{(y,s)} \rightarrow 0, \quad y \rightarrow \infty \tag{21}$$

Table 3. Numerical variation of the thermal, concentration, and momentum fields.

<i>y</i>	Temp by Stehfest	Temp by Stehfest	Conc by Tzou	Conc by Tzou	Vel by Stehfest	Vel by Tzou
0.1	0.702	0.733	0.795	0.801	0.684	0.681
0.3	0.480	0.489	0.501	0.514	0.553	0.547
0.5	0.328	0.326	0.314	0.328	0.414	0.407
0.7	0.224	0.217	0.196	0.209	0.296	0.289
0.9	0.153	0.144	0.121	0.132	0.206	0.199
1.1	0.104	0.095	0.074	0.083	0.141	0.134
1.3	0.071	0.063	0.044	0.052	0.095	0.089
1.5	0.049	0.041	0.026	0.032	0.063	0.059
1.7	0.033	0.027	0.015	0.022	0.042	0.038
1.9	0.023	0.018	0.009	0.012	0.028	0.024

Table 4. Numerical influence of different constraints on the Nusselt number, Sherwood number, and the skin friction.

α	φ	<i>t</i>	<i>Pr/Sc</i>	<i>Nu</i>	<i>Sh</i>	<i>C_f</i>
0.1	0.02	0.6	4.7	1.856	1.640	1.230
0.2	0.02	0.6	4.7	1.773	1.709	1.105
0.3	0.02	0.6	4.7	1.708	1.776	1.012
0.2	0.01	0.6	4.7	1.521	1.694	0.380
0.2	0.02	0.6	4.7	1.353	1.598	0.163
0.2	0.03	0.6	4.7	1.270	1.576	0.059
0.2	0.02	0.5	4.7	1.523	2.014	0.562
0.2	0.02	0.6	4.7	1.473	2.071	0.163
0.2	0.02	0.7	4.7	1.418	2.135	0.059
0.2	0.02	0.6	4.5	1.521	1.694	0.380
0.2	0.02	0.6	4.6	1.353	1.598	0.163
0.2	0.02	0.6	4.7	1.270	1.576	0.059

Inserting Equation (20) into (19) and applying the above-transformed conditions, the concentration field will be

$$\bar{C}_{(\xi,s)} = \frac{1}{s} e^{-\xi \sqrt{\frac{Sc s^{1-\beta}}{(1-\alpha s^{-\alpha})^\gamma}}} \tag{22}$$

Again the Laplace inverse of the above-attained solution will be performed, numerically, in Tables 3 and 4.

4.3. Solution for the Velocity Profile

This section examines the semi-analytical solution of the momentum profile with its physically transformed conditions. Bearing in mind the result of Equation (13), employing the LT on Equation (6), the non-homogeneous ordinary differential equation from the momentum field will be as follows

$$\Lambda_1 \frac{\partial^2 \bar{w}(y,s)}{\partial y^2} - \left(\Lambda_2 M \sin(\theta_1) + \frac{\Lambda_1}{K} + \Lambda_o(s + \beta_1) \right) \bar{w}(y,s) = -\Lambda_3 \cos(\theta_2) \bar{T}(y,s) - \Lambda_4 \cos(\theta_2) \bar{C}(y,s) \tag{23}$$

$$\bar{w}(0,s) - \frac{\partial \bar{w}(y,s)}{\partial y} \Big|_{y=0} = F(s); \quad \bar{w}(y,s) \rightarrow 0 \text{ as } y \rightarrow \infty$$

By interpolating the above-considered conditions and simplifying Equation (20), the momentum profile will be

$$\bar{w}(y,s) = \frac{1}{1+h\sqrt{\frac{1}{\Lambda_1}(\Pi_3+\Lambda_o s)}} \left(\frac{\Pi_5}{\Lambda_1 s \left(\sqrt{\frac{\Pi_4 s}{s^\beta(1-as^{-\alpha})^\gamma} - 1} \right)} \frac{1+h\sqrt{\frac{\Lambda_5 Pr}{\Lambda_6} \frac{s}{s^\beta(1-as^{-\alpha})^\gamma}}}{\left(\frac{\Pi_4 s}{s^\beta(1-as^{-\alpha})^\gamma} \right) - \frac{1}{\Lambda_1}(\Pi_3+\Lambda_o s)} + \frac{\Pi_6}{\Lambda_1 s} \frac{1+h\sqrt{\frac{Sc s}{s^\beta(1-as^{-\alpha})^\gamma}}}{\left(\frac{Sc s}{s^\beta(1-as^{-\alpha})^\gamma} \right) - \frac{1}{\Lambda_1}(\Pi_3+\Lambda_o s)} + F(s) \right) e^{-y\sqrt{\frac{1}{\Lambda_1}(\Pi_3+\Lambda_o s)}} \tag{24}$$

$$- \frac{\Pi_5}{\Lambda_1 s \left(\sqrt{\frac{\Pi_4 s}{s^\beta(1-as^{-\alpha})^\gamma} - 1} \right)} \frac{e^{-y\sqrt{\frac{\Pi_4 s}{s^\beta(1-as^{-\alpha})^\gamma}}}}{\left(\frac{\Pi_4 s}{s^\beta(1-as^{-\alpha})^\gamma} \right) - \frac{1}{\Lambda_1}(\Pi_3+\Lambda_o s)} - \frac{\Pi_6}{\Lambda_1 s} \frac{e^{-y\sqrt{\frac{Sc s}{s^\beta(1-as^{-\alpha})^\gamma}}}}{\left(\frac{Sc s}{s^\beta(1-as^{-\alpha})^\gamma} \right) - \frac{1}{\Lambda_1}(\Pi_3+\Lambda_o s)}$$

where

$$\Pi_1 = \Lambda_2 M \sin(\theta_1), \quad \Pi_2 = \frac{\Lambda_1}{K} + \Lambda_o \beta_1, \quad \Pi_3 = \Pi_1 + \Pi_2,$$

$$\Pi_4 = \frac{\Lambda_5 Pr}{\Lambda_6}, \quad \Pi_5 = \Lambda_3 Gr \cos(\theta_2), \quad \Pi_6 = \Lambda_4 Gm \cos(\theta_2)$$

We can't find the inverse transform analytically in the complex transform spaces for several real-world applications. To produce the inverse Laplace, authors have also employed specific numerical techniques. Many scholars have successfully applied Stehfest's technique and Tzou's [58] for the numerical Laplace method, to solve the fractional differential equations, efficiently and effectively. The formula for the Stehfest and Tzou algorithms is as follows, respectively:

$$f(y,t) = \frac{\ln(2)}{t} \sum_{n=1}^{2N} h_n \bar{f} \left(y, n \frac{\ln(2)}{t} \right)$$

where N is a positive integer.

$$h_n = (-1)^{n+\frac{N}{2}} \sum_{r=\lfloor \frac{p+1}{2} \rfloor}^{\min(p,N)} \frac{r^N (2r)!}{(N-r)! r! (r-1)! (p-r)! (2r-p)!}$$

and

$$f(y,t) = \frac{e^{4.7}}{t} \left[\frac{1}{2} \bar{f} \left(r, \frac{4.7}{t} \right) + \operatorname{Re} \left\{ \sum_{j=1}^N (-1)^j \bar{f} \left(r, \frac{4.7 + k\pi i}{t} \right) \right\} \right]$$

Limiting Case:

If, in the attained solution of the momentum field Equation (21), the physical quantities $Gm = Sc = K = 0, \theta_1 = \frac{\pi}{2}$ become zero, then

$$\bar{w}(y,s) = \frac{1}{1+h\sqrt{\frac{1}{\Lambda_1}(\Pi_3+\Lambda_o s)}} \left(\frac{\Pi_5}{\Lambda_1 s \left(\sqrt{\frac{\Pi_4 s}{s^\beta(1-as^{-\alpha})^\gamma} - 1} \right)} \frac{1+h\sqrt{\frac{\Pi_4 s}{s^\beta(1-as^{-\alpha})^\gamma}}}{\left(\frac{\Pi_4 s}{s^\beta(1-as^{-\alpha})^\gamma} \right) - \frac{1}{\Lambda_1}(\Pi_3+\Lambda_o s)} + F(s) \right) e^{-y\sqrt{\frac{1}{\Lambda_1}(\Pi_3+\Lambda_o s)}} \tag{25}$$

$$- \frac{\Pi_5}{\Lambda_1 s \left(\sqrt{\frac{\Pi_4 s}{s^\beta(1-as^{-\alpha})^\gamma} - 1} \right)} \frac{e^{-y\sqrt{\frac{\Pi_4 s}{s^\beta(1-as^{-\alpha})^\gamma}}}}{\left(\frac{\Pi_4 s}{s^\beta(1-as^{-\alpha})^\gamma} \right) - \frac{1}{\Lambda_1}(\Pi_3+\Lambda_o s)}$$

The above-attained solution of the velocity profile is quite similar to the attained solution by Saqib et al. [45]. Furthermore, the Prabhakar fractional constraints β, γ can be taken as zero for the generalized results of the governed equations.

Special Cases:

The following are essential exceptional cases, with a technical significance that is widely recognized and well defined in the existing literature to understand the problem better.

Case 1: $f(t) = \text{Sin}(\omega t)$

In the first particular case, consider the function $f(t) = \text{Sin}(\omega t)$, in which ω signifies the amplitude of the oscillating plate, then the momentum profile for this case will be

$$\bar{w}(y,s) = \frac{1}{1+h\sqrt{\frac{1}{\Lambda_1}(\Pi_3+\Lambda_0s)}} \left(\frac{\Pi_5}{\Lambda_1s \left(\sqrt{\frac{\Pi_4s}{s^\beta(1-as^{-\alpha})^\gamma} - 1} \right)} \frac{1+h\sqrt{\frac{\Lambda_5Pr}{\Lambda_6} \frac{s}{s^\beta(1-as^{-\alpha})^\gamma}}}{\left(\frac{\Pi_4s}{s^\beta(1-as^{-\alpha})^\gamma} \right) - \frac{1}{\Lambda_1}(\Pi_3+\Lambda_0s)} + \frac{\Pi_6}{\Lambda_1s} \frac{1+h\sqrt{\frac{Scs}{s^\beta(1-as^{-\alpha})^\gamma}}}{\left(\frac{Scs}{s^\beta(1-as^{-\alpha})^\gamma} \right) - \frac{1}{\Lambda_1}(\Pi_3+\Lambda_0s)} + \frac{\omega}{\omega^2+s^2} \right) e^{-y\sqrt{\frac{1}{\Lambda_1}(\Pi_3+\Lambda_0s)}} - \frac{\Pi_5}{\Lambda_1s \left(\sqrt{\frac{\Pi_4s}{s^\beta(1-as^{-\alpha})^\gamma} - 1} \right)} \frac{e^{-y\sqrt{\frac{\Pi_4s}{s^\beta(1-as^{-\alpha})^\gamma}}}}{\left(\frac{\Pi_4s}{s^\beta(1-as^{-\alpha})^\gamma} \right) - \frac{1}{\Lambda_1}(\Pi_3+\Lambda_0s)} - \frac{\Pi_6}{\Lambda_1s} \frac{e^{-y\sqrt{\frac{Scs}{s^\beta(1-as^{-\alpha})^\gamma}}}}{\left(\frac{Scs}{s^\beta(1-as^{-\alpha})^\gamma} \right) - \frac{1}{\Lambda_1}(\Pi_3+\Lambda_0s)} \tag{26}$$

Case 2: $f(t) = \text{Cos}(\omega t)$

In the second particular case, consider the function $f(t) = \text{Cos}(\omega t)$, then the momentum profile for this case will be

$$\bar{w}(y,s) = \frac{1}{1+h\sqrt{\frac{1}{\Lambda_1}(\Pi_3+\Lambda_0s)}} \left(\frac{\Pi_5}{\Lambda_1s \left(\sqrt{\frac{\Pi_4s}{s^\beta(1-as^{-\alpha})^\gamma} - 1} \right)} \frac{1+h\sqrt{\frac{\Lambda_5Pr}{\Lambda_6} \frac{s}{s^\beta(1-as^{-\alpha})^\gamma}}}{\left(\frac{\Pi_4s}{s^\beta(1-as^{-\alpha})^\gamma} \right) - \frac{1}{\Lambda_1}(\Pi_3+\Lambda_0s)} + \frac{\Pi_6}{\Lambda_1s} \frac{1+h\sqrt{\frac{Scs}{s^\beta(1-as^{-\alpha})^\gamma}}}{\left(\frac{Scs}{s^\beta(1-as^{-\alpha})^\gamma} \right) - \frac{1}{\Lambda_1}(\Pi_3+\Lambda_0s)} + \frac{q}{\omega^2+s^2} \right) e^{-y\sqrt{\frac{1}{\Lambda_1}(\Pi_3+\Lambda_0s)}} - \frac{\Pi_5}{\Lambda_1s \left(\sqrt{\frac{\Pi_4s}{s^\beta(1-as^{-\alpha})^\gamma} - 1} \right)} \frac{e^{-y\sqrt{\frac{\Pi_4s}{s^\beta(1-as^{-\alpha})^\gamma}}}}{\left(\frac{\Pi_4s}{s^\beta(1-as^{-\alpha})^\gamma} \right) - \frac{1}{\Lambda_1}(\Pi_3+\Lambda_0s)} - \frac{\Pi_6}{\Lambda_1s} \frac{e^{-y\sqrt{\frac{Scs}{s^\beta(1-as^{-\alpha})^\gamma}}}}{\left(\frac{Scs}{s^\beta(1-as^{-\alpha})^\gamma} \right) - \frac{1}{\Lambda_1}(\Pi_3+\Lambda_0s)} \tag{27}$$

Case 3: $f(t) = te^t$

In the third particular case, consider the function $f(t) = te^t$ having its Laplace $F(s) = \frac{1}{(s-1)^2}$, then the momentum field for this case will be

$$\bar{w}(y,s) = \frac{1}{1+h\sqrt{\frac{1}{\Lambda_1}(\Pi_3+\Lambda_0s)}} \left(\frac{\Pi_5}{\Lambda_1s \left(\sqrt{\frac{\Pi_4s}{s^\beta(1-as^{-\alpha})^\gamma} - 1} \right)} \frac{1+h\sqrt{\frac{\Lambda_5Pr}{\Lambda_6} \frac{s}{s^\beta(1-as^{-\alpha})^\gamma}}}{\left(\frac{\Pi_4s}{s^\beta(1-as^{-\alpha})^\gamma} \right) - \frac{1}{\Lambda_1}(\Pi_3+\Lambda_0s)} + \frac{\Pi_6}{\Lambda_1s} \frac{1+h\sqrt{\frac{Scs}{s^\beta(1-as^{-\alpha})^\gamma}}}{\left(\frac{Scs}{s^\beta(1-as^{-\alpha})^\gamma} \right) - \frac{1}{\Lambda_1}(\Pi_3+\Lambda_0s)} + \frac{1}{(s-1)^2} \right) e^{-y\sqrt{\frac{1}{\Lambda_1}(\Pi_3+\Lambda_0s)}} - \frac{\Pi_5}{\Lambda_1s \left(\sqrt{\frac{\Pi_4s}{s^\beta(1-as^{-\alpha})^\gamma} - 1} \right)} \frac{e^{-y\sqrt{\frac{\Pi_4s}{s^\beta(1-as^{-\alpha})^\gamma}}}}{\left(\frac{\Pi_4s}{s^\beta(1-as^{-\alpha})^\gamma} \right) - \frac{1}{\Lambda_1}(\Pi_3+\Lambda_0s)} - \frac{\Pi_6}{\Lambda_1s} \frac{e^{-y\sqrt{\frac{Scs}{s^\beta(1-as^{-\alpha})^\gamma}}}}{\left(\frac{Scs}{s^\beta(1-as^{-\alpha})^\gamma} \right) - \frac{1}{\Lambda_1}(\Pi_3+\Lambda_0s)} \tag{28}$$

Validity of the Fractional Model

Both numerical approaches, Stehfest’s and Tzou’s, were compared by drawing Figure 2a,b for the concentration and temperature profiles. There is a slight overlap of the findings between the two curves. Figure 3a,b compares both numerical methods and solutions for the velocity field, using the Prabhakar fractional methodology with Saqib et al. [42]. The simulations obtained by employing the Prabhakar fractional model have a good accuracy, compared to Saqib et al.’s study [42].

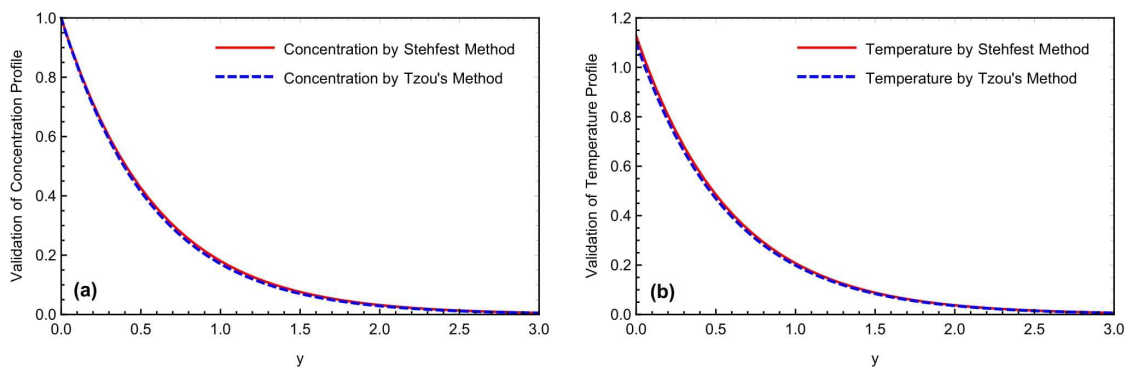


Figure 2. (a,b) Comparison of the numerical schemes for the concentration and temperature fields.

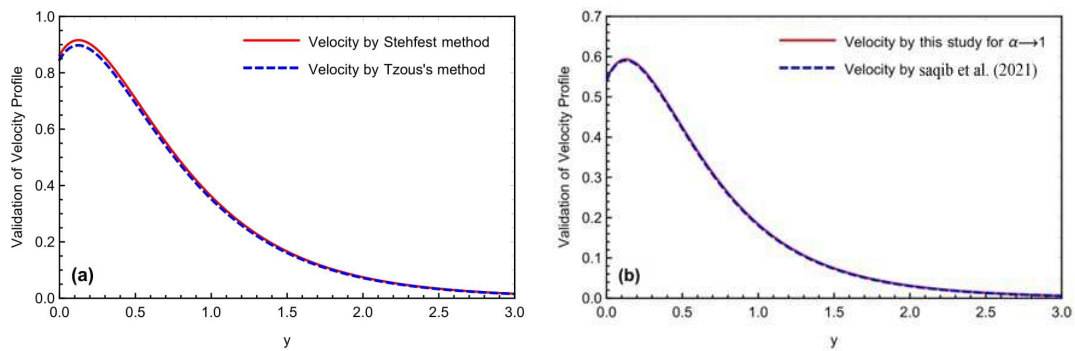


Figure 3. (a,b) Comparison of the numerical schemes and Saqjib et al. [42], for the momentum field.

5. Results with Discussion

The mixed convection Brinkman-type nanofluid model’s thermal study, due to an oscillating inclined plate in an applied magnetic field, is examined using fractional simulations. Different nanoparticles, i.e., molybdenum disulfide (MOs_2) and graphene-oxide (GO) are utilized for the nanofluid with a base engine oil fluid. A close thermal inspection of the modified nanofluid model is provided using molybdenum disulfide and graphene oxide nanoparticles with a viscoelastic base fluid. In the preceding part, the Prabhakar fractional derivative framework was successfully executed for the solution of the governed fractional equations. Some exceptional cases for the momentum profile are also described, improving the flowing fluid’s physical significance. The physical impact of the different constraints on the thermal, concentration, and momentum profiles are also analyzed graphically in Figures 4–11, with different nanoparticles and different ranges, such as $0.1 < \alpha, \beta, \gamma < 0.9$, $4 < Gr < 16$, $0.01 < \varphi < 0.04$, $0.5 < \omega < 2.0$, $2.0 < Gm < 10$, $0.5 < K < 2.0$, $0.5 < M < 2.0$ and $0.1 < Sc < 1.5$. This section outlined the thermal dynamics of the flow model when the flow parameters were varied.

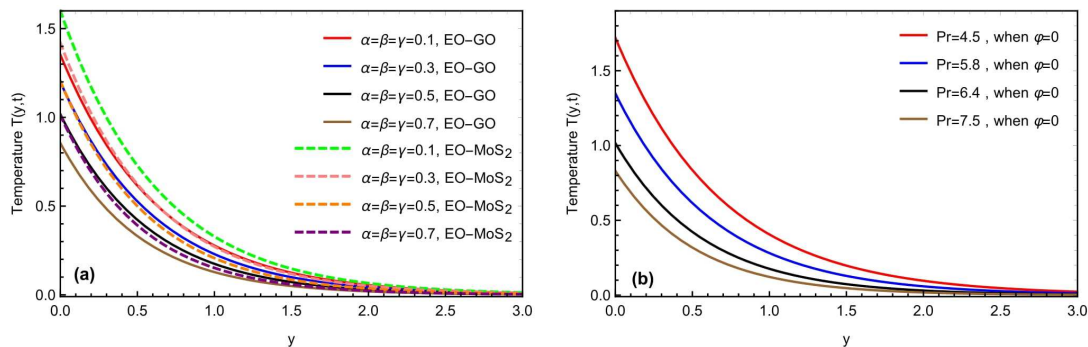


Figure 4. (a,b) Consequence of the fractional constraints and Pr on the temperature field.

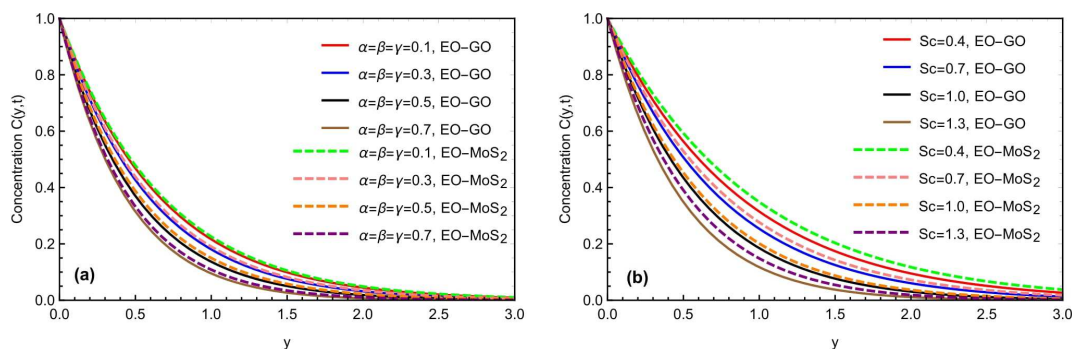


Figure 5. (a,b) Consequence of the fractional constraints and Sc on the concentration field.

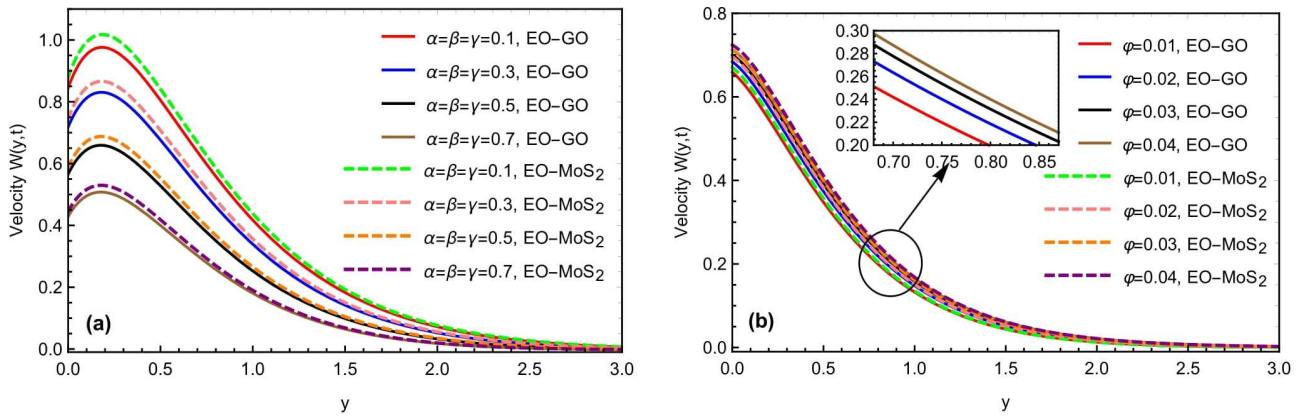


Figure 6. (a,b) Consequence of α, β, γ , and φ on the momentum profile with $Sc = 1.2, Gr = 10.4, Gm = 8.2, M = 1.5, K = 0.7, h = 0.5, \theta_1 = \theta_2 = \frac{\pi}{4}, t = 0.9$.

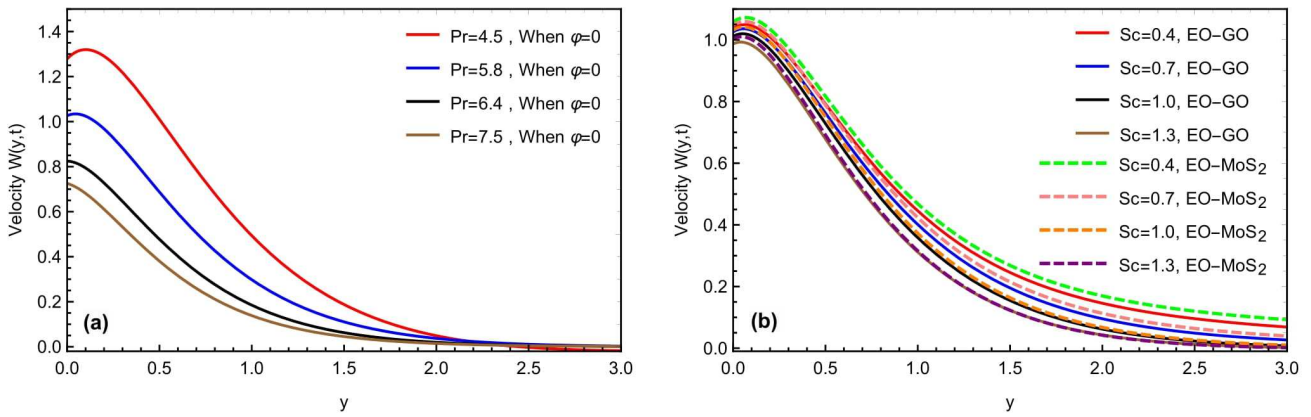


Figure 7. (a,b) Consequence of Pr and Sc on the momentum profile with $\alpha = \beta = \gamma = 0.8, Gr = 10.4, Gm = 8.2, M = 1.5, K = 0.7, h = 0.5, \theta_1 = \theta_2 = \frac{\pi}{4}, t = 0.9$.

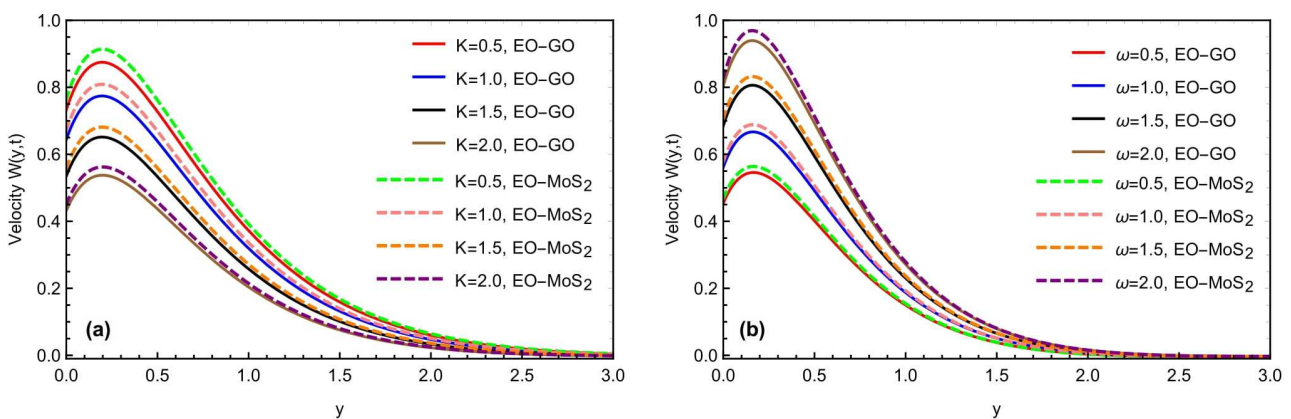


Figure 8. (a,b) Consequence of K and ω on the momentum profile with $\alpha = \beta = \gamma = 0.8, Sc = 1.2, M = 1.5, Gr = 10.4, Gm = 8.2, K = 0.7, h = 0.5, \theta_1 = \theta_2 = \frac{\pi}{4}, t = 0.9$.

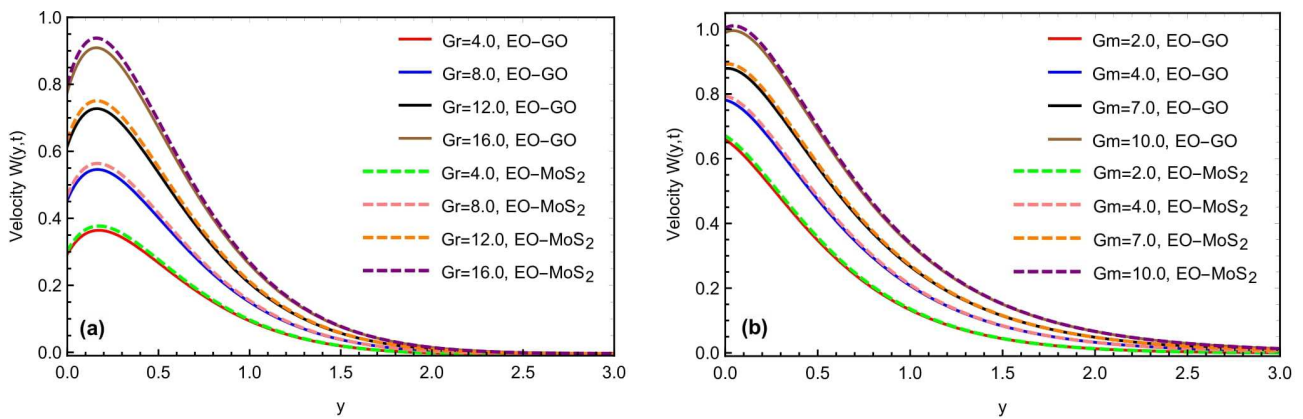


Figure 9. (a,b) Consequence of Gr and Gm on the momentum profile with $\alpha = \beta = \gamma = 0.8, Sc = 1.2, M = 1.5, K = 0.7, h = 0.5, \theta_1 = \theta_2 = \frac{\pi}{4}, t = 0.9$.

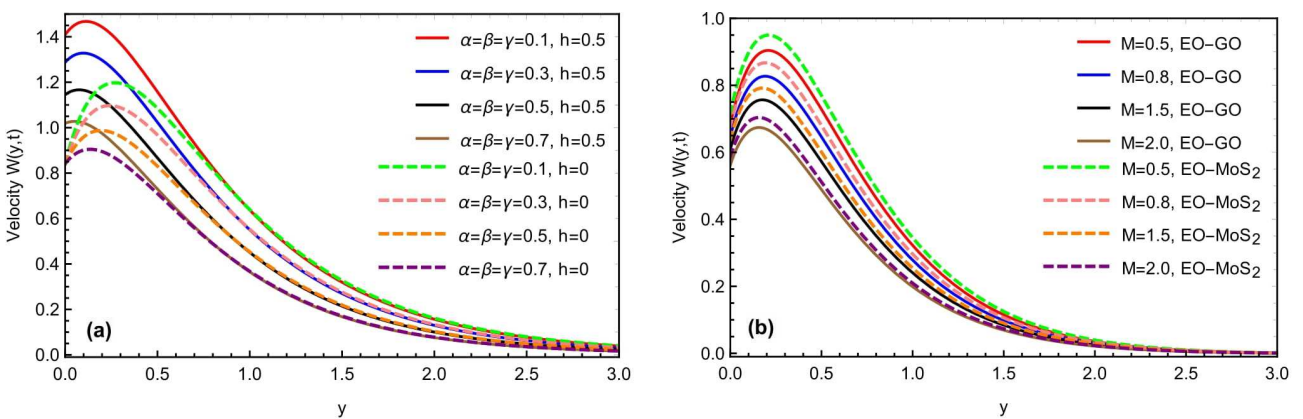


Figure 10. (a,b) Consequence of h and M on the momentum profile with $\alpha = \beta = \gamma = 0.8, Sc = 1.2, Gr = 10.4, Gm = 8.2, K = 0.7, \theta_1 = \theta_2 = \frac{\pi}{4}, t = 0.9$.

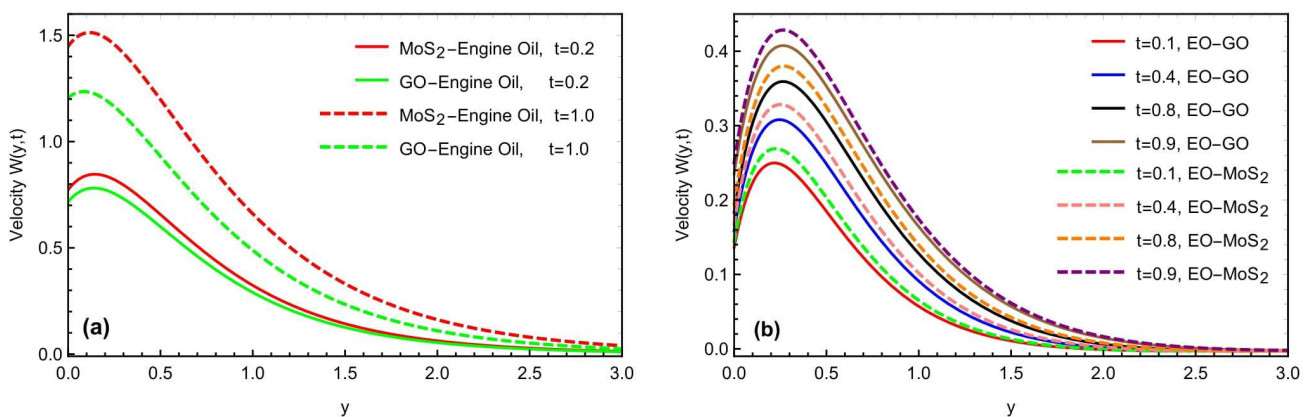


Figure 11. (a,b) Consequence of time t and comparison of the different nanofluids with the different nanoparticles.

Figure 4a,b shows how the fractional restrictions (α, β, γ) and the Prandtl number Pr affect the temperature profile. The thermal properties of the molybdenum disulfide-engine oil ($MOS_2 - EO$) and the graphene oxide-engine oil ($GO - EO$) nanofluids are compared. By changing (α, β, γ), the temperature profile for both $MOS_2 - EO$ and ($GO - EO$) nanomaterial suspensions showed a declining tendency. The thermal profile nearer the plate

is maximal for the lower values of the fractional parameters, while the most significant fall in the profile is seen for the bigger values. The higher values of (α, β, γ) related to the thickness of the thermal and momentum boundary layers represent the physical point. The higher values of reducing (α, β, γ) the thickness of the thermal boundary layer, result in a declining trend in the temperature and velocity profiles. Moreover, the improvement in thermal rate, due to $MOS_2 - EO$ is more progressive, as compared to $GO - EO$, due to the physical characteristics of the selected nanoparticles. Figure 4b conveys the effects of Pr , showing a declining change in the temperature field. Mathematically, as Pr is the ratio of the kinematic viscosity to the thermal diffusivity and, physically, varying the value of the Prandtl number, the thermal conductivity reduces, and the fluid becomes thicker, due to which the temperature reduces, as depicted in Figure 4b. Figure 5a,b indicates the impact of the fractional constraints α, β, γ , and the Schmidt number Sc on the boundary layer concentration for both types of nanofluids ($MOS_2 - EO$) and ($GO - EO$). Again, similar to the thermal profile, the concentration field also decays by increasing the fractional constraints and Schmidt number values. Physically, the molecular diffusivity will decrease with the Schmidt number values' enhancement. Furthermore, with the thermal field, the concentration profile also declares more values in the graphical representation for the molybdenum disulfide (MOS_2) based nanofluid, as compared to the graphene oxide (GO) mixed suspension.

Figure 6a,b highlights the physical impact of the fractional constraints α, β, γ and the volume fraction on the momentum field for both the molybdenum disulfide-engine oil ($MOS_2 - EO$) and graphene oxide-engine oil ($GO - EO$) type nanofluids. Increasing the values of (α, β, γ) , lowers the mobility of the EO-based nanofluid, due to a decrease in the thickness of the momentum barrier layer. Assigning the variation in the fractional parameters, the fluid motion slows down. Moreover, with the variation in the volume fraction parameters, the velocity profile is improved, due to the effective density of the considered nanoparticles. The fluid velocity is also improved for the (MOS_2) based nanoparticles, as compared to the (GO) suspension, due to the heat conduction. As the volume fraction increases, the fluid becomes more viscous, indicating that the GO nanoparticles' fluid velocity will decrease, owing to the heat conduction. These novel observations may present many applications in improving the thermal capacitance of various engineering and industrial processes. Figure 7a,b predicts the influence of the Prandtl number Pr and the Schmidt number Sc on the momentum profile of the Brinkman-type nanofluid. The flowing rate is observed as the decreasing value for both parameters Pr and Sc . As the enhancement in Pr creates some more hinderances and increases the flowing fluid viscosity, it results in a decrement in the fluid velocity, and the fluid flows more slowly. Similarly, similar to the impact of the Prandtl number, the Schmidt number also slows down the fluid motion, due to a decrement in the diffusivity rate of the flowing fluid. It is concluded that the velocity profile of the nanoparticles (GO) decreases while approaching the plate, but the velocity of the nanoparticles (MoS_2) rises owing to the nanoparticle features.

The graphical impact of the porosity parameter K and the effects of the oscillations of the inclined plate, is represented in Figure 8a,b. For the general function $f(t)$, we have considered the function $Sin(\omega t)$ as a particular function, where ω represents the frequency of the oscillations. Moreover, this can be seen that the fluid flow moves fast with the increment in the frequency of the oscillations. Figure 9a,b depicts the graphical behavior of the heat Grashof number Gr and the mass Grashof number Gm on a velocity profile. The velocity profile has been enhanced with large values of Gr and Gm . Physically, the heat Grashof number Gr creates natural convection, owing to the buoyant force, and an increase in the Gm improves the buoyancy forces, increasing the fluid velocity. This is the weighted average of the buoyancy and viscous forces. A higher Gr generates an increase in the buoyant forces, which causes the generated flows to increase. Figure 10a,b depicts the impact of the slip parameter h and the magnetic number M on the fluid velocity. The velocity field was reduced by raising the magnetic parameter value. Physically, an increase in the magnetic field results in an increase in the Lorentz force, which decreases the velocity

of the fluid. Furthermore, the maximum effect of the Lorentz forces is when the angle of inclination of the applied magnetics is at the right angle to the oscillating plate. M is a dimensionless number associated with the Lorentz force, which opposes the nanofluid velocity. The more excellent the M , the greater the Lorentz force, which resists motion. As a result, the velocity was slowed in both cases of the engine oil-based nanofluid with the increasing M . Similarly, the inclination of a magnetic field reduces the influence of M on the Lorentz force. The Lorentz force has the most significant impact at $\theta_1 = \pi/2$ (normal magnetic field), as seen in the figures. While the slip parameter h improved, the fluid motion and momentum field increased with the enhancement in the slip factor, as predicted in the figures. Figure 11a,b predicts the comparative change in the flow rate with the interaction of all types of nanoparticles MOS_2 and GO with the engine oil as based liquid and the effects of time t on the momentum field. It is interesting to note that the interaction of the MOS_2 nanoparticles are more practical in improving the flowing fluid rate, as compared to the GO nanoparticles. The addition of the different nanoparticles means an enhancement in the fluid density, increasing the flowing nanofluid's thickness. Therefore, the (GO) nanoparticle-based suspension of the nanofluid has a lower flowing rate, as compared to the (MOS_2) nanoparticles mixed with the nanofluid. Furthermore, as illustrated in Figure 11b, the thickness of the boundary layer grows thicker than the thickness of the momentum boundary layer with time, thus enhancing the fluid motion.

Finally, the numerical analysis of the temperature, concentration, and velocity profiles by Stehfest's and Tzou's numerical schemes, is analyzed in Table 3. To validate our numerical inverse Laplace, transform solutions using Stehfest's and Tzou's methods, we performed numerical calculations for the temperature and velocity fields, which were found to be in good agreement, as shown in Table 3. The temperature profile, concentration, and momentum fields declined as they moved away from the inclined plate with the increasing y and became zero for $y \rightarrow \infty$, which signifies the boundary conditions. Furthermore, in the numerical analysis of both Stehfest's and Tzou's algorithms, very closed values of all governed parameters by the different numerical techniques, also validate this study. At instant rises, the decreasing change in the heat transmission and mass transfer is progressive. According to Table 4, the local Nusselt number and the wall shear force decreased as it increased, indicating a significant agreement for the temperature profile. Table 5 also shows the percentage difference in the momentum field analysis.

Table 5. Comparison of the momentum field with the work of Saqib et al. [42] when $\alpha, \beta, \gamma \rightarrow 1$.

y	Velocity by This Study	Velocity by Saqib et al. [42]	Percentage Difference of both Velocities
0.1	0.887	0.901	0.086%
0.3	0.764	0.771	0.107%
0.5	0.604	0.608	0.127%
0.7	0.457	0.458	0.181%
0.9	0.337	0.336	0.248%
1.1	0.244	0.243	0.272%
1.3	0.176	0.174	0.267%
1.5	0.126	0.124	0.244%
1.7	0.089	0.083	0.214%
1.9	0.064	0.063	0.182%

6. Conclusions

The fractional-supported Brinkman-type nanofluid was examined using different nanoparticles and an oscillating inclined poured plate. Molybdenum disulfide and graphene

oxide nanoparticles with a viscoelastic base liquid are investigated to increase the thermal performance. The motivations for implementing the Prabhakar-like fractional model are justified, as this fractional algorithm contains modern definitions without any restriction of singularities. The correctness of the fractional scheme is checked by setting up a comparison task with another fractional approach, and several unique and limiting circumstances are given to obtain the physical insight into the examined fractional model. Finally, the thermal determination of the used molybdenum-disulfide (MoS_2) and graphene-oxide (GO) nanoparticles are depicted in comparison. The following are the most critical findings from the present model:

- The fractional parameters α, β, γ declined the thermal, concentration, and momentum profiles for the $MoS_2 - EO$ and $GO - EO$ nanoparticle suspension and the rate decrement are thicker as the time instants increase.
- The heat transfer rate for both nanoparticles susceptible to the engine oil base material may be regulated for the specific Prandtl number values.
- Because of the thermal conductivity factor, the thermal performances of the molybdenum disulfide MoS_2 nanoparticles with engine oil base fluid are more progressive than the graphene oxide GO nanoparticles.
- The changing velocity is caused by the variations in the heat and mass Grashof constants for the molybdenum disulfide engine oil and the graphene oxide engine oil suspensions.
- Using the Prabhakar operators with the fractional coefficient's parameter settings, might help to select an appropriate computational formula that produces a good consistency between the experimental and theoretical values.
- In the graphical comparison of the attained solution of the momentum profile with Saqib et al. [42], the overlapping of both curves validates the attained results of this study.
- Implementing the Prabhakar fractional derivative technique is also a powerful tool to simulate the analytical expressions for any coupled and nonlinear partial differential system.
- The patterns and characteristics of all physical flow metrics coincide perfectly with the published studies.
- The overlaying of both curves in assessing both numerical techniques confirms the obtained solutions of the governed equations.

Our computational effort has effectively clarified the parametric implications of the flow of two different nanoparticle phases. The results for the two different nanoparticles show significant monotonic differences. This study might be expanded to three or more hybrid phases to identify which hybrid phase is the most effective.

Author Contributions: Conceptualization, S.M.E., A.R., B.C.P. and U.K.; methodology, B.C.P., S.M.E., A.R. and U.K.; software, B.C.P., S.M.E., A.R., N.A. and U.K.; validation, B.C.P., S.M.E., A.R., U.K., S.E. and A.M.A. (Ahmed M. Abed); formal analysis, A.M.A. (Abeer M. Alotaibi), S.E., A.R., A.M.A. (Ahmed M. Abed) and N.A.; investigation, U.K., A.M.A. (Abeer M. Alotaibi), S.E., N.A. and A.M.A. (Ahmed M. Abed); resources, A.M.A. (Abeer M. Alotaibi); data curation, N.A.; writing—original draft preparation, U.K., A.M.A. (Abeer M. Alotaibi), S.E. and A.M.A. (Ahmed M. Abed); writing—review and editing, N.A., A.M.A. (Abeer M. Alotaibi) and A.M.A. (Ahmed M. Abed); visualization, N.A., A.R., A.M.A. (Ahmed M. Abed) and S.E.; supervision, B.C.P.; project administration, S.M.E.; funding acquisition, S.M.E. and N.A. All authors have read and agreed to the published version of the manuscript.

Funding: The author expresses her gratitude to the Princess Nourah bint Abdulrahman University Researchers Supporting Project number (PNURSP2022R163), Princess Nourah bint Abdulrahman University, Riyadh, Saudi Arabia.

Data Availability Statement: Not applicable.

Acknowledgments: The present work was supported by the Princess Nourah bint Abdulrahman University Researchers Supporting Project number (PNURSP2022R163), Princess Nourah bint Abdulrahman University, Riyadh, Saudi Arabia.

Conflicts of Interest: The authors declare no conflict of interest.

Nomenclatures

w -	Velocity [m/s]
t -	Time [s]
U_0 -	Constant velocity [m/s]
T -	Temperature [K]
T_∞ -	Temperature of fluid away from the plate [K]
T_w -	Fluids temperature at the plate [K]
C -	Concentration of the fluid [Kg m^{-3}]
C_w -	Fluids concentration at the plate [Kg m^{-3}]
C_p -	Specific heat at constant pressure [$\text{J Kg}^{-1} \text{K}^{-1}$]
g -	Acceleration due to gravity [m/s^2]
D -	Mass diffusion coefficient [$\text{m}^2 \text{s}^{-1}$]
Sc -	Schmidt number []
β_1 -	Casson fluid parameter []
h -	Slip parameter [-]
Gr -	Heat Grashof number [-]
ν_f -	Kinematic viscosity [m^2/s]
μ -	Dynamic viscosity [$\text{Kg m}^{-1} \text{s}^{-1}$]
σ -	Electrical conductivity [S/m]
θ_2 -	Angle of inclination of the plate [-]
α, β, γ Prabhakar	Fractional derivative operators [-]
θ_1 -	Angle of inclination of magnetic field [-]
Pr -	Prandtl number [-]
K -	Porosity parameter [-]
Gm -	Mass Grashof number [-]
s -	Laplace transformed variable [-]
Nu -	Nusselt number [-]
C_f -	Skin friction [-]

Note: This [-] represents the dimensionless quantity.

References

- Gumber, P.; Yaseen, M.; Rawat, S.K.; Kumar, M. Heat transfer in micropolar hybrid nanofluid flow past a vertical plate in the presence of thermal radiation and suction/injection effects. *Partial. Differ. Equ. Appl. Math.* **2022**, *5*, 100240. [[CrossRef](#)]
- Aliseda, A.; Hopfinger, E.J.; Lasheras, J.C.; Kremer, D.; Berchielli, A.; Connolly, E. Atomization of viscous and non-Newtonian liquids by a coaxial, high-speed gas jet. Experiments and droplet size modeling. *Int. J. Multiph. Flow* **2008**, *34*, 161–175. [[CrossRef](#)]
- Lissant, K.J. Non-Newtonian Pharmaceutical Compositions. U.S. Patent 4,040,857, 9 August 1977.
- Muskat, M. The flow of homogeneous fluids through porous media. JW Edwards. *Inc. Ann Arbor, Michigan* **1946**, *763*, 100.
- Brinkman, H.C. On the permeability of media consisting of closely packed porous particles. *Flow Turbul. Combust.* **1949**, *1*, 81–86. [[CrossRef](#)]
- Neale, G.; Nader, W. Practical significance of Brinkman's extension of Darcy's law: Coupled parallel flows within a channel and a bounding porous medium. *Can. J. Chem. Eng.* **1974**, *52*, 475–478. [[CrossRef](#)]
- Jie, Z.; Ijaz Khan, M.; Al-Khaled, K.; El-Zahar, E.R.; Acharya, N.; Raza, A.; Khan, S.U.; Xia, W.F.; Tao, N.X. Thermal transport model for Brinkman type nanofluid containing carbon nanotubes with sinusoidal oscillations conditions: A fractional derivative concept. *Waves Random Complex Media* **2022**, 1–20. [[CrossRef](#)]
- Raza, A.; Ghaffari, A.; Khan, S.U.; Haq, A.U.; Khan, M.I.; Khan, M.R. Non-singular fractional computations for the radiative heat and mass transfer phenomenon subject to mixed convection and slip boundary effects. *Chaos Solitons Fractals* **2022**, *155*, 111708. [[CrossRef](#)]
- Sadripour, S. 3D numerical analysis of atmospheric-aerosol/carbon-black nanofluid flow within a solar air heater located in Shiraz, Iran. *Int. J. Numer. Methods Heat Fluid Flow* **2018**, *29*, 1378–1402. [[CrossRef](#)]
- Shateyi, S.; Prakash, J. A new numerical approach for MHD laminar boundary layer flow and heat transfer of nanofluids over a moving surface in the presence of thermal radiation. *Bound. Value Probl.* **2014**, *2014*, 2. [[CrossRef](#)]

11. Srivastava, H.; Dubey, V.; Kumar, R.; Singh, J.; Kumar, D.; Baleanu, D. An efficient computational approach for a fractional-order biological population model with carrying capacity. *Chaos Solitons Fractals* **2020**, *138*, 109880. [[CrossRef](#)]
12. Kumar, S.; Gómez-Aguilar, J.F. Numerical solution of Caputo-Fabrizio time fractional distributed order reaction-diffusion equation via quasi wavelet based numerical method. *J. Appl. Comput. Mech.* **2020**, *6*, 848–861.
13. Mahanthesh, B. Flow and heat transport of nanomaterial with quadratic radiative heat flux and aggregation kinematics of nanoparticles. *Int. Commun. Heat Mass Transf.* **2021**, *127*, 105521. [[CrossRef](#)]
14. Rana, P.; Mahanthesh, B.; Mackolil, J.; Al-Kouz, W. Nanofluid flow past a vertical plate with nanoparticle aggregation kinematics, thermal slip and significant buoyancy force effects using modified Buongiorno model. *Waves Random Complex Media* **2021**, 1–25. [[CrossRef](#)]
15. Mishra, S.; Mahanthesh, B.; Mackolil, J.; Pattnaik, P.K. Nonlinear radiation and cross-diffusion effects on the micropolar nanoliquid flow past a stretching sheet with an exponential heat source. *Heat Transfer* **2021**, *50*, 3530–3546. [[CrossRef](#)]
16. Swain, K.; Mahanthesh, B. Thermal enhancement of radiating magneto-nanoliquid with nanoparticles aggregation and joule heating: A three-dimensional flow. *Arab. J. Sci. Eng.* **2021**, *46*, 5865–5873. [[CrossRef](#)]
17. Abro, K.A.; Khan, I.; Gomez-Aguilar, J. Heat transfer in magnetohydrodynamic free convection flow of generalized ferrofluid with magnetite nanoparticles. *J. Therm. Anal. Calorim.* **2021**, *143*, 3633–3642. [[CrossRef](#)]
18. Turkyilmazoglu, M. On the transparent effects of Buongiorno nanofluid model on heat and mass transfer. *Eur. Phys. J. Plus* **2021**, *136*, 376. [[CrossRef](#)]
19. Jabbaripour, B.; Rostami, M.N.; Dinarvand, S.; Pop, I. Aqueous aluminium–copper hybrid nanofluid flow past a sinusoidal cylinder considering three-dimensional magnetic field and slip boundary condition. *Proc. Inst. Mech. Eng. Part E J. Process Mech. Eng.* **2021**. [[CrossRef](#)]
20. Raza, A.; Khan, U.; Almusawa, M.; Hamali, W.; Galal, A.M. Prabhakar-fractional simulations for the exact solution of Casson-type fluid with experiencing the effects of magneto-hydrodynamics and sinusoidal thermal conditions. *Int. J. Mod. Phys. B* **2022**. [[CrossRef](#)]
21. Izady, M.; Dinarvand, S.; Pop, I.; Chamkha, A.J. Flow of aqueous Fe₂O₃–CuO hybrid nanofluid over a permeable stretching/shrinking wedge: A development on Falkner–Skan problem. *Chin. J. Phys.* **2021**, *74*, 406–420. [[CrossRef](#)]
22. Gómez-Aguilar, J.F.; ur Rahman, G.; Javed, M. Stability analysis for fractional order implicit ψ -Hilfer differential equations. *Math. Methods Appl. Sci.* **2022**, *45*, 2701–2712.
23. Mackolil, J.; Mahanthesh, B. Computational simulation of surface tension and gravitation-induced convective flow of a nanoliquid with cross-diffusion: An optimization procedure. *Appl. Math. Comput.* **2022**, *425*, 127108. [[CrossRef](#)]
24. Bafakeeh, O.T.; Raza, A.; Khan, S.U.; Khan, M.I.; Nasr, A.; Khedher, N.B.; Tag-Eldin, E.S.M. Physical Interpretation of Nanofluid (Copper Oxide and Silver) with Slip and Mixed Convection Effects: Applications of Fractional Derivatives. *Appl. Sci.* **2022**, *12*, 10860. [[CrossRef](#)]
25. Khan, S.U.; Usman; Raza, A.; Kanwal, A.; Javid, K. Mixed convection radiated flow of Jeffery-type hybrid nanofluid due to inclined oscillating surface with slip effects: A comparative fractional model. *Waves Random Complex Media* **2022**, 1–22. [[CrossRef](#)]
26. Shafee, A.; Arabkoohsar, A.; Sheikholeslami, M.; Jafaryar, M.; Ayani, M.; Nguyen-Thoi, T.; Basha, D.B.; Tlili, I.; Li, Z. Numerical simulation for turbulent flow in a tube with combined swirl flow device considering nanofluid exergy loss. *Phys. A Stat. Mech. Its Appl.* **2020**, *542*, 122161. [[CrossRef](#)]
27. Farshad, S.A.; Sheikholeslami, M. Numerical examination for entropy generation of turbulent nanomaterial flow using complex turbulator in a solar collector. *Phys. A: Stat. Mech. Its Appl.* **2020**, *550*, 123951. [[CrossRef](#)]
28. Hussanan, A.; Khan, I.; Hashim, H.; Anuar, M.K.; Ishak, N.; Sarif, N.M.; Salleh, M.Z. Unsteady MHD flow of some nanofluids past an accelerated vertical plate embedded in a porous medium. *J. Teknol.* **2016**, *78*, 121–126. [[CrossRef](#)]
29. Sheikholeslami, M.; Zia, Q.Z.; Ellahi, R. Influence of induced magnetic field on free convection of nanofluid considering Koo-Kleinstreuer-Li (KKL) correlation. *Appl. Sci.* **2016**, *6*, 324. [[CrossRef](#)]
30. Akyürek, E.F.; Geliş, K.; Şahin, B.; Manay, E. Experimental analysis for heat transfer of nanofluid with wire coil turbulators in a concentric tube heat exchanger. *Results Phys.* **2018**, *9*, 376–389. [[CrossRef](#)]
31. Khan, M.I.; Raza, A.; Naseem, M.; Al-Khaled, K.; Khan, S.U.; Khan, M.I.; El-Zahar, E.R.; Malik, M.Y. Comparative analysis for radiative slip flow of magnetized viscous fluid with mixed convection features: Atangana-Baleanu and Caputo-Fabrizio fractional simulations. *Case Stud. Therm. Eng.* **2021**, *28*, 101682. [[CrossRef](#)]
32. Raza, A.; Khan, S.U.; Khan, M.I.; El-Zahar, E.R. Heat Transfer Analysis for Oscillating Flow of Magnetized Fluid by Using the Modified Prabhakar-Like Fractional Derivatives. *Res. Sq.* **2021**. [[CrossRef](#)]
33. Tian, Y.; Zhong, L.-F.; He, G.-T.; Yu, T.; Luo, M.-K.; Stanley, H.E. The resonant behavior in the oscillator with double fractional-order damping under the action of nonlinear multiplicative noise. *Phys. A Stat. Mech. Its Appl.* **2018**, *490*, 845–856. [[CrossRef](#)]
34. Rathore, N. Darcy–Forchheimer and Ohmic heating effects on GO-TiO₂ suspended cross nanofluid flow through stenosis artery. *Proc. Inst. Mech. Eng. Part C J. Mech. Eng. Sci.* **2022**, 236. [[CrossRef](#)]
35. Mabood, F.; Ashwinkumar, G.; Sandeep, N. Effect of nonlinear radiation on 3D unsteady MHD stagnancy flow of Fe₃O₄/graphene–water hybrid nanofluid. *Int. J. Ambient. Energy* **2022**, *43*, 3385–3395. [[CrossRef](#)]
36. Sandeep, N. Effect of aligned magnetic field on liquid thin film flow of magnetic-nanofluids embedded with graphene nanoparticles. *Adv. Powder Technol.* **2017**, *28*, 865–875. [[CrossRef](#)]
37. Rosa, C.; de Oliveira, E.C. Relaxation equations: Fractional models. *J. Phys. Math.* **2015**, *6*, 1–7.

38. Atangana, A.; Baleanu, D. New fractional derivatives with nonlocal and non-singular kernel: Theory and application to heat transfer model. *arXiv* **2016**, arXiv:1602.03408. [[CrossRef](#)]
39. Wang, Y.; Mansir, I.B.; Al-Khaled, K.; Raza, A.; Khan, S.U.; Khan, M.I.; Ahmed, A.E.S. Thermal outcomes for blood-based carbon nanotubes (SWCNT and MWCNTs) with Newtonian heating by using new Prabhakar fractional derivative simulations. *Case Stud. Therm. Eng.* **2022**, *32*, 101904. [[CrossRef](#)]
40. Mahanthesh, B.; Brizlyn, T.; Shehzad, S.; Gireesha, B. Nonlinear thermo-solutal convective flow of Casson fluid over an oscillating plate due to non-coaxial rotation with quadratic density fluctuation: Exact solutions. *Multidiscip. Model. Mater. Struct.* **2019**, *15*, 818–842. [[CrossRef](#)]
41. Abro, K.A.; Mirbhar, M.N.; Gomez-Aguilar, J. Functional application of Fourier sine transform in radiating gas flow with non-singular and non-local kernel. *J. Braz. Soc. Mech. Sci. Eng.* **2019**, *41*, 400. [[CrossRef](#)]
42. Saqib, M.; Khan, I.; Shafie, S.; Mohamad, A.Q.; Sherif, E.-S.M. Analysis of magnetic resistive flow of generalized Brinkman type nanofluid containing carbon nanotubes with ramped heating. *Comput Mater Contin* **2021**, *67*, 1069–1084. [[CrossRef](#)]
43. Khan, H.; Gómez-Aguilar, J.; Khan, A.; Khan, T.S. Stability analysis for fractional order advection–reaction diffusion system. *Phys. A Stat. Mech. Its Appl.* **2019**, *521*, 737–751. [[CrossRef](#)]
44. Abro, K.A.; Khan, I.; Gómez-Aguilar, J. Thermal effects of magnetohydrodynamic micropolar fluid embedded in porous medium with Fourier sine transform technique. *J. Braz. Soc. Mech. Sci. Eng.* **2019**, *41*, 174. [[CrossRef](#)]
45. Siddiqui, A.A.; Turkyilmazoglu, M. A new theoretical approach of wall transpiration in the cavity flow of the ferrofluids. *Micromachines* **2019**, *10*, 373. [[CrossRef](#)] [[PubMed](#)]
46. Pandey, P.; Kumar, S.; Gómez, F. Approximate analytical solution of two-dimensional space-time fractional diffusion equation. *Math. Methods Appl. Sci.* **2020**, *43*, 7194–7207. [[CrossRef](#)]
47. Ahokposi, D.; Atangana, A.; Vermeulen, D. Modelling groundwater fractal flow with fractional differentiation via Mittag-Leffler law. *Eur. Phys. J. Plus* **2017**, *132*, 165. [[CrossRef](#)]
48. Khan, I.; Shah, N.A.; Vieru, D. Unsteady flow of generalized Casson fluid with fractional derivative due to an infinite plate. *Eur. Phys. J. Plus* **2016**, *131*, 181. [[CrossRef](#)]
49. Khan, I.; Shah, N.A.; Mahsud, Y.; Vieru, D. Heat transfer analysis in a Maxwell fluid over an oscillating vertical plate using fractional Caputo-Fabrizio derivatives. *Eur. Phys. J. Plus* **2017**, *132*, 194. [[CrossRef](#)]
50. Shah, N.A.; Vieru, D.; Fetecau, C. Effects of the fractional order and magnetic field on the blood flow in cylindrical domains. *J. Magn. Magn. Mater.* **2016**, *409*, 10–19. [[CrossRef](#)]
51. Mahanthesh, B.; Mackolil, J. Flow of nanoliquid past a vertical plate with novel quadratic thermal radiation and quadratic Boussinesq approximation: Sensitivity analysis. *Int. Commun. Heat Mass Transf.* **2021**, *120*, 105040. [[CrossRef](#)]
52. Ahmad, M.; Asjad, M.I.; Nisar, K.S.; Khan, I. Mechanical and thermal energies transport flow of a second grade fluid with novel fractional derivative. *Proc. Inst. Mech. Eng. Part E J. Process Mech. Eng.* **2021**. [[CrossRef](#)]
53. Ghalib, M.M.; Zafar, A.A.; Riaz, M.B.; Hammouch, Z.; Shabbir, K. Analytical approach for the steady MHD conjugate viscous fluid flow in a porous medium with nonsingular fractional derivative. *Phys. A Stat. Mech. Its Appl.* **2020**, *554*, 123941. [[CrossRef](#)]
54. Fallah, B.; Dinarvand, S.; Yazdi, M.E.; Rostami, M.N.; Pop, I. MHD flow and heat transfer of SiC-TiO₂/DO hybrid nanofluid due to a permeable spinning disk by a novel algorithm. *J. Appl. Comput. Mech.* **2019**, *5*, 976–988.
55. Arif, M.; Kumam, P.; Khan, D.; Watthayu, W. Thermal performance of GO-MoS₂/engine oil as Maxwell hybrid nanofluid flow with heat transfer in oscillating vertical cylinder. *Case Stud. Therm. Eng.* **2021**, *27*, 101290. [[CrossRef](#)]
56. Basit, A.; Asjad, M.I.; Akgül, A. Convective flow of a fractional second grade fluid containing different nanoparticles with Prabhakar fractional derivative subject to non-uniform velocity at the boundary. *Math. Methods Appl. Sci.* **2021**. [[CrossRef](#)]
57. Kolsi, L.; Raza, A.; Al-Khaled, K.; Ghachem, K.; Khan, S.U.; Haq, A.U. Thermal applications of copper oxide, silver, and titanium dioxide nanoparticles via fractional derivative approach. *Waves Random Complex Media* **2022**, 1–14. [[CrossRef](#)]
58. Riaz, M.B.; Siddique, I.; Saeed, S.T.; Atangana, A. MHD Oldroyd-B Fluid with Slip Condition in view of Local and Nonlocal Kernels. *J. Appl. Comput. Mech.* **2020**. [[CrossRef](#)]